

## 2D FORCE CONSTRAINTS IN THE METHOD OF REGULARIZED STOKESLETS \*

ONDREJ MAXIAN<sup>†</sup> AND WANDA STRYCHALSKI<sup>‡</sup>

**Abstract.** For many biological systems that involve elastic structures immersed in fluid, small length scales mean that inertial effects are also small, and the fluid obeys the Stokes equations. One way to solve the model equations representing such systems is through the Stokeslet, the fundamental solution to the Stokes equations, and its regularized counterpart, which treats the singularity of the velocity at points where force is applied. In two dimensions, an additional complication arises from Stokes' paradox, whereby the velocity from the Stokeslet is unbounded at infinity when the net hydrodynamic force within the domain is nonzero, invalidating the solutions. A straightforward computationally inexpensive method is presented for obtaining valid solutions to the Stokes equations for net nonzero forcing. The approach is based on imposing a mean zero velocity condition on a large curve that surrounds the domain of interest. The condition is shown to be equivalent to a net-zero force condition, where the opposite forces are applied on the large curve. The numerical method is applied to models of cellular motility and blebbing.

**Key words.** fluid-structure interaction, Stokes flow, Stokes' paradox, regularized Stokeslets

**AMS subject classifications.** 65M80, 74F10, 92C37

**1. Introduction.** Stokes flow refers to the regime of viscous flow where inertial effects are small, and the Navier-Stokes equations simplify to the Stokes equations. For fluid-structure interaction problems in cell biology, such as an elastic red blood cell membrane deforming in capillary flow [1, 2], the small length scales of the cell diameter ( $\sim 10 \mu\text{m}$ ) lead to a small Reynolds number. Other important biological phenomena in cell biology that involve zero Reynolds number flow are cell motility [3, 4, 5] and organism swimming [6, 7].

Because the Stokes equations are linear, boundary integral and boundary element methods can be used to determine the velocity and pressure fields that come from a collection of forces [8, 9]. The velocity field generated from a point force is known as a *Stokeslet*. One problem that arises when using the Stokeslet in practice is the singularity at the point where the force arises. For closed interfaces, this singularity is integrable, but careful numerical quadratures are necessary to correctly calculate the velocity and pressure [8, 9]. In [10], Cortez introduced the method of regularized Stokeslets to overcome the singularities in both the pressure and velocity expressions for forces located at scattered points. Instead of the force being applied at a point, the force is applied over a small ball of radius  $\epsilon$ . The regularized Stokeslet and pressure expressions are then obtained analytically from the particular function used to represent the small ball. The method of regularized Stokeslets can also be used for closed surfaces, bypassing the associated issues with numerical quadrature [8].

Another problem that arises when modeling fluid flow in two dimensional domains with Stokeslets is that the velocity is *unbounded* at infinity when there is a nonzero net hydrodynamic force acting within the domain of flow, contradicting the assumption

---

\*Submitted to the editors June 18th, 2018.

**Funding:** This work was supported by a grant from the Simons Foundation (#429808, Wanda Strychalski).

<sup>†</sup>Department of Chemical and Biomolecular Engineering and Department of Mathematics, Applied Mathematics, and Statistics, Case Western Reserve University, Cleveland, OH 44106, U.S.A. (oxm60@case.edu)

<sup>‡</sup>Department of Mathematics, Applied Mathematics, and Statistics, Case Western Reserve University, Cleveland, OH 44106, U.S.A. (wis6@case.edu)

in the derivation of the Stokeslet that the velocity is zero at infinity [8, 10, 11]. The problem is therefore ill-posed, and numerical simulations of such systems lead to unphysical spurious velocities. The phenomenon of unbounded velocities in systems with nonzero net force, especially as  $|\boldsymbol{x}| \rightarrow \infty$ , is usually referred to as Stokes' paradox [4]. We emphasize that this is a unique feature of Stokes flow in 2D. In 3D, the problem is well-posed; the Stokeslet decays to zero at infinity regardless of the net forcing, so the boundary condition is satisfied and the solution is valid for any collection of forces with bounded magnitude.

In 2D, one way to ensure that the velocity profile is valid within a bounded domain is to enforce a boundary condition within the region of interest. The method of regularized Stokeslets was employed in [10] to simulate the flow due to a cylinder moving at an imposed velocity. In [12, 13, 14], the method of images was used to add additional Stokeslets outside of the flow domain that enforce a zero boundary condition near a plane wall. In these approaches, there is an additional constraint on the *velocity* that leads to valid solutions near the immersed objects of interest. However, if no boundary conditions within the flow domain are specified by the model of the physical system (e.g. when modeling flexible fibers in Stokes flow [15, 16, 17]), a different approach must be used.

One such approach is to enforce a constraint on the *force* rather than the velocity, in particular that the net hydrodynamic force over the entire domain be zero. Sometimes, this constraint comes naturally, such as in models of flagellar swimming [18] or fibers immersed in a background flow [16]. However, the only *a priori* requirement of fluid-structure interaction in Stokes flow is that the hydrodynamic force at a point is exactly balanced by the internal and external forces on the immersed structures [19]. Our primary motivation arises from cell biology, where the internal cytoskeleton is constantly out of equilibrium due to polymerization of filaments and ATP hydrolysis of molecular motors, which promotes configuration changes [20]. In models that involve cytoskeletal dynamics, internal and external force imbalances may arise when polymerization/contractile stresses are treated en masse, and a net nonzero hydrodynamic force results. A nonzero net force is also more ubiquitous than just in cell biology; for example, Cortez's model of a moving cylinder [10] had a nonzero net hydrodynamic force within the domain of flow.

Teran and Peskin [21] treated the problem of unbalanced forces within the immersed boundary method [22, 23] by adding a unique, constant, velocity throughout the periodic domain to ensure that the net force is zero for all time. In that formulation, an additional constant velocity is permitted because the equations are simulated on a periodic domain, where the solution is unique up to a constant. In this case, it is required that the net force be zero [24]. The net zero force requirement in a periodic IB method presents some challenges. For example, tether forces *must* be introduced in the domain in order to simulate body forces (as the authors did in [21] when modeling peristaltic pumping). In order for the immersed structures to remain stationary, the tether spring stiffness must be large, which in turn increases the overall stiffness of the numerical scheme and the cost of the IB method formulation as a whole.

We present a method to simulate models in 2D Stokes flow with net nonzero forcing using the method of regularized Stokeslets. We accomplish this by fusing the two boundary conditions together: we surround the domain by a large circle and constrain the *mean velocity* on the circle to be zero. As the radius of the circle goes to infinity, this constraint becomes equivalent to a net zero force constraint within an infinite domain. In this way, we avoid placing additional forces at arbitrary points in the domain, thereby preserving the pressure and velocity dynamics in the region

of interest. In addition, we show that a mean zero velocity at the large circle can be achieved simply by adding a constant velocity throughout a large domain of flow, thereby avoiding linear systems on the large circle (as in [4]). This observation results in an algorithm that is very straightforward to implement. After presenting our method in Sections 2 and 3, we show in Section 4 how it can be applied to 2D models of cells immersed in Stokes flow.

**2. Mathematical framework.** The steady Stokes equations in two dimensions are

$$(2.1) \quad \mu \Delta \mathbf{u} - \nabla p = -\mathbf{f}$$

$$(2.2) \quad \nabla \cdot \mathbf{u} = 0,$$

where  $\mu$  is the fluid viscosity,  $p$  is the pressure,  $\mathbf{u}$  is the fluid velocity, and  $\mathbf{f}$  is the hydrodynamic force, exactly equal to the external applied force that comes from fibers or other structures immersed in the fluid [19]. We begin by summarizing the method of regularized Stokeslets [10] for computing  $\mathbf{u}$  and  $p$  from Eqs. (2.1) and (2.2). Then we present the modification for addressing Stokes' paradox.

**2.1. Method of regularized Stokeslets.** In the method of regularized Stokeslets, a force of strength  $\mathbf{f}_0$  is distributed over a small ball centered on a point  $\mathbf{x}_0$ , so that

$$(2.3) \quad \mathbf{f}(\mathbf{x}) = \mathbf{f}_0 \phi_\epsilon(\mathbf{x} - \mathbf{x}_0).$$

The Stokes equations can be solved with the force in Eq. (2.3) to derive the resulting velocity and pressure from a given ‘‘blob’’ or ‘‘cutoff’’ function  $\phi_\epsilon$ . For example, if

$$(2.4) \quad \phi_\epsilon(\mathbf{x}) = \frac{3\epsilon^3}{2\pi(\|\mathbf{x}\|^2 + \epsilon)^{5/2}},$$

then

$$(2.5) \quad p^\epsilon(\mathbf{x}, \mathbf{x}_0) = \frac{1}{2\pi} (\mathbf{f}_0 \cdot (\mathbf{x} - \mathbf{x}_0)) \left( \frac{r_0^2 + 2\epsilon^2 + \epsilon\sqrt{r_0^2 + \epsilon^2}}{(\sqrt{r_0^2 + \epsilon^2} + \epsilon)(r_0^2 + \epsilon^2)^{3/2}} \right)$$

and

$$(2.6) \quad \mathbf{u}^\epsilon(\mathbf{x}, \mathbf{x}_0) = -\frac{\mathbf{f}_0}{4\pi\mu} \left( \ln \left( \sqrt{r_0^2 + \epsilon^2} + \epsilon \right) - \frac{\epsilon(\sqrt{r_0^2 + \epsilon^2} + 2\epsilon)}{(\sqrt{r_0^2 + \epsilon^2} + \epsilon)\sqrt{r_0^2 + \epsilon^2}} \right) \\ + \frac{1}{4\pi\mu} (\mathbf{f}_0 \cdot (\mathbf{x} - \mathbf{x}_0)) (\mathbf{x} - \mathbf{x}_0) \frac{\sqrt{r_0^2 + \epsilon^2} + 2\epsilon}{(\sqrt{r_0^2 + \epsilon^2} + \epsilon)^2 \sqrt{r_0^2 + \epsilon^2}}$$

are the pressure and velocity that result from the force in Eq. (2.3), where  $r_0 = \|\mathbf{x} - \mathbf{x}_0\|$ . The derivation of these expressions can be found in [10]. Notice that for  $r_0 \gg \epsilon$ , the standard Stokeslet expressions [8] are recovered,

$$(2.7) \quad p(\mathbf{x}, \mathbf{x}_0) = \frac{\mathbf{f}_0 \cdot (\mathbf{x} - \mathbf{x}_0)}{2\pi r_0^2},$$

$$(2.8) \quad \mathbf{u}(\mathbf{x}, \mathbf{x}_0) = -\frac{\mathbf{f}_0}{4\pi\mu} \ln(r_0) + (\mathbf{f}_0 \cdot (\mathbf{x} - \mathbf{x}_0)) \frac{(\mathbf{x} - \mathbf{x}_0)}{4\pi\mu r_0^2}.$$

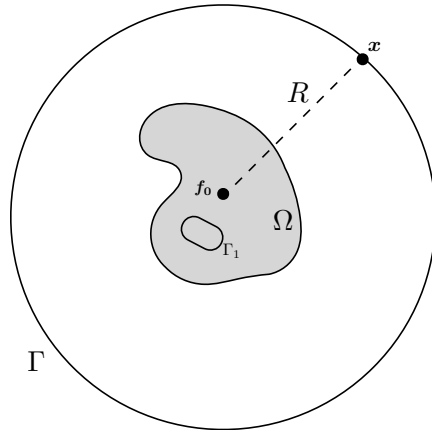


FIG. 1.  $\Omega$  denotes the region bounding immersed interfaces and/or point forces.  $\Gamma_1$  indicates an immersed interface and  $\mathbf{f}_0$  denotes a point force at  $\mathbf{x}_0$  enclosed by  $\Omega$ . A circle of radius  $R$  is denoted by  $\Gamma$ .

The pressure and velocity resulting from a collection of forces  $\mathbf{f}_k$  spread over a collection of points  $\mathbf{x}_k$  is simply a superposition of the results from Eqs. (2.3) - (2.5). It is easier to see that if  $\sum_k \mathbf{f}_k \neq \mathbf{0}$ , the velocity in Eq. (2.6) or (2.8) is unbounded at infinity, and the boundary conditions  $\mathbf{u} \rightarrow \mathbf{0}$  are not satisfied at infinity.

**2.2. Modification for nonzero net force.** Suppose that all of the forces  $\mathbf{f}_k$  and immersed interfaces in a model system are located within a domain  $\Omega$  (see Fig. 1). We note that  $\Omega$  is not necessarily an immersed interface, but rather a sort of “bounding box” in which all of the forces are contained. If there are no other boundary conditions within  $\Omega$ , such as a specified velocity on a curve  $\Gamma_1$  contained within the domain, the problem is ill-posed and the solution for the velocity in Eq. (2.6) is not valid, even near  $\Omega$ . To construct a mathematically valid solution inside some space containing  $\Omega$ , we surround  $\Omega$  with a large circle, denoted by  $\Gamma$  with radius  $R$  (illustrated in Fig. 1). One approach from [4] is to enforce a zero velocity boundary condition at every point on the discretized circle. A linear system obtained from Eq. (2.6) can be solved for the forces required to obtain a zero velocity on the large circle. Those forces can then be used in Eq. (2.6) to compute the velocity at locations enclosed by the smaller domain  $\Omega$ . We note that this requires a linear system to be solved at each time value when simulating a model of a dynamic process.

We take a slightly different approach. Instead of requiring  $\mathbf{u}|_{\Gamma} = \mathbf{0}$  at every point, we impose a slightly weaker condition, that the average value of  $\mathbf{u}$  on  $\Gamma$ ,  $\langle \mathbf{u} \rangle_{\Gamma} = \mathbf{0}$ . Notice that as  $R \rightarrow \infty$ , the velocity on the large circle is approximately *constant* because of the dominance of the radially symmetric first term in Eq. (2.8). If the velocity at the large circle is constant, the two conditions are equivalent. Imposing the mean velocity condition leads us to add an extra velocity  $\mathbf{u}^R$  throughout the domain so that the average velocity on the large circle is zero.

We begin by deriving the velocity  $\mathbf{u}^R$  in the case of a single point force followed by the generalization to multiple forces by superposition. Let  $\mathbf{f}_0$  be the force at a point  $\mathbf{x}_0$  in  $\Omega$ . Let  $\mathbf{x}$  be a point on the large circle  $\Gamma$  (see Fig. 1), and let  $r_0 = \|\mathbf{x} - \mathbf{x}_0\|$ .

Since  $\mathbf{x}$  is on a large circle with arbitrarily large radius  $R$ ,  $r_0(\mathbf{x}) \gg \epsilon$  for all  $\mathbf{x} \in \Gamma$ , and we can represent the velocity at the large circle using the standard Stokeslet. Thus

$$(2.9) \quad \mathbf{u}(\mathbf{x}, \mathbf{x}_0) = -\frac{\mathbf{f}_0}{4\pi\mu} \ln(r_0) + (\mathbf{f}_0 \cdot (\mathbf{x} - \mathbf{x}_0)) \frac{\mathbf{x} - \mathbf{x}_0}{4\pi\mu r_0^2},$$

is the velocity at  $\mathbf{x}$  due to the force  $\mathbf{f}_0$  applied at  $\mathbf{x}_0$ .

Using  $s$  as the arclength parameter and treating  $r_0 = R$  as constant, the average value of  $\mathbf{u}(\mathbf{x}, \mathbf{x}_0)$  is

$$(2.10)$$

$$\langle \mathbf{u}(\mathbf{x}, \mathbf{x}_0) \rangle = \frac{1}{2\pi R} \int_{\Gamma} \left( -\frac{\mathbf{f}_0}{4\pi\mu} \ln(r_0) + (\mathbf{f}_0 \cdot (\mathbf{x} - \mathbf{x}_0)) \frac{\mathbf{x} - \mathbf{x}_0}{4\pi\mu r_0^2} \right) ds$$

$$(2.11) \quad = \frac{1}{2\pi R} \left( -\frac{\mathbf{f}_0}{4\pi\mu} \ln R \int_{\Gamma} ds + \frac{1}{4\pi\mu R^2} \int_{\Gamma} (\mathbf{f}_0 \cdot (\mathbf{x} - \mathbf{x}_0)) (\mathbf{x} - \mathbf{x}_0) ds \right)$$

$$(2.12) \quad = -\frac{\mathbf{f}_0}{4\pi\mu} \ln R + \left( \frac{1}{2\pi R} \right) \frac{1}{4\pi\mu R^2} \int_{\Gamma} (\mathbf{f}_0 \cdot (\mathbf{x} - \mathbf{x}_0)) (\mathbf{x} - \mathbf{x}_0) ds.$$

The last equality used the fact that  $\int_{\Gamma} ds = 2\pi R$ . Computing the second integral, we begin by changing to an angle parameterization of  $\Gamma$  via  $s = R\theta$ ,

$$(2.13) \quad \frac{1}{2\pi R} \int_{\Gamma} (\mathbf{f}_0 \cdot (\mathbf{x} - \mathbf{x}_0)) (\mathbf{x} - \mathbf{x}_0) ds = \frac{1}{2\pi R} \int_0^{2\pi} (\mathbf{f}_0 \cdot (\mathbf{x} - \mathbf{x}_0)) (\mathbf{x} - \mathbf{x}_0) R d\theta$$

Because the circle is rotation invariant, we can place the  $x$  axis on the same direction as  $\mathbf{f}_0$  without loss of generality. Therefore, let  $\mathbf{f}_0 = f \begin{pmatrix} 1 \\ 0 \end{pmatrix}$ . Furthermore, in the limit

$R \rightarrow \infty$ ,  $\mathbf{x} - \mathbf{x}_0 = \mathbf{x} = \begin{pmatrix} R \cos \theta \\ R \sin \theta \end{pmatrix}$ . Then Eq. (2.13) simplifies to

$$(2.14) \quad \frac{1}{2\pi R} \int_0^{2\pi} (\mathbf{f}_0 \cdot (\mathbf{x} - \mathbf{x}_0)) (\mathbf{x} - \mathbf{x}_0) R d\theta = \frac{1}{2\pi} \int_0^{2\pi} f R \cos \theta \begin{pmatrix} R \cos \theta \\ R \sin \theta \end{pmatrix} d\theta$$

$$(2.15) \quad = \frac{R^2 f}{2} \begin{pmatrix} 1 \\ 0 \end{pmatrix} = \frac{R^2 \mathbf{f}_0}{2}.$$

Substituting Eq. (2.15) into Eq. (2.12), we have the average velocity over the large circle given the force  $\mathbf{f}_0$  at  $\mathbf{x}_0$  as

$$(2.16) \quad \langle \mathbf{u}(\mathbf{x}, \mathbf{f}_0) \rangle = \frac{\mathbf{f}_0}{4\pi\mu} \left( \frac{1}{2} - \ln R \right).$$

Our goal is to impose the boundary condition that the *mean velocity on the large circle is zero*. It follows immediately that this can be done by subtracting the constant velocity in Eq. (2.16) throughout the domain of flow. The additional velocity due to a point force  $\mathbf{f}_0$  is therefore

$$(2.17) \quad \mathbf{u}^R(\mathbf{f}_0) = -\frac{\mathbf{f}_0}{4\pi\mu} \left( \frac{1}{2} - \ln R \right).$$

In the case of multiple forces  $\mathbf{f}_k$  (for example, forces that come from an interface such as  $\Gamma_1$  in Fig. 1), the constant velocity is simply the superposition of velocities from Eq. (2.17).

$$(2.18) \quad \mathbf{u}^R = \sum_{k=1}^N \mathbf{u}^R(\mathbf{f}_k) = \sum_{k=1}^N -\frac{\mathbf{f}_k}{4\pi\mu} \left( \frac{1}{2} - \ln R \right).$$

This velocity is added throughout the domain of flow to ensure that  $\langle \mathbf{u} \rangle_\Gamma = 0$ . Because the velocity on  $\Gamma$  is approximately constant, we have ensured a zero flow boundary condition on  $\Gamma$ , and therefore the validity of the solution within the domain  $\Omega$  enclosed by  $\Gamma$ .

It is no coincidence that Eq. (2.18) expresses the average value of the velocity due to forces of strength  $-\mathbf{f}_k$ . By adding the constant velocity in Eq. (2.18), we are effectively adding a force on the large circle that *has the effect of adding an equal and opposite force within the region of interest  $\Omega$* . Meanwhile, the addition of a constant velocity throughout the domain results in a relative velocity profile that is unchanged from that computed by Eq. (2.6). This is in contrast to the addition of more Stokeslets at arbitrary locations in the domain  $\Omega$ , the latter being problematic because the relative local profile (and subsequent physical conclusions) are dependent on the locations of the additional Stokeslets.

Finally, the addition of this constant velocity has no effect on the pressure profile calculated from Eq. (2.5). Because a constant velocity is added, no pressure gradient is generated within the domain. Equivalently, our addition of a constant velocity is a shortcut around explicitly adding forces on the large circle that enforce the zero boundary condition exactly (e.g. [4]). Due to the nature of the pressure solution in Eq. (2.5) (i.e. that it decays as  $1/r_0$ ), these additional “forces” on the large circle have no effect on the local pressure profile for large  $R$ .

**3. Discretization.** In general, we begin with a collection of  $N$  points  $\mathbf{x}_k$  with forces  $\mathbf{f}_k$  in some domain  $\Omega$ . At each timestep, we compute the velocity of each point as

$$(3.1) \quad \mathbf{u}(\mathbf{x}_i) = \mathbf{u}^R + \sum_{k=1}^N \mathbf{u}^\epsilon(\mathbf{x}_i, \mathbf{x}_k),$$

where  $\mathbf{u}^R$  is given by Eq. (2.18) and  $\mathbf{u}^\epsilon(\mathbf{x}_i, \mathbf{x}_k)$  is given by Eq. (2.6). Because  $\mathbf{u}^R$  is constant throughout the domain, the calculation in Eq. (3.1) is  $\mathcal{O}(2N + (2N)^2)$ . The first  $\mathcal{O}(2N)$  operations arise from the computation of the constant additional velocity in Eq. (2.18). The second  $\mathcal{O}((2N)^2)$  operations come from computing the regularized velocities in Eq. (2.6) for all of the points.

We compare this operation count to alternative formulations. Suppose that the large circle was discretized with  $M$  points and the forces on the large circle solved for explicitly, as in [4]. This calculation is a  $2M \times 2M$  linear solve and requires  $\mathcal{O}((2M)^2)$  operations using GMRES. In addition, the calculation of the added velocities at each point in the domain from the forces on the large circle requires another  $\mathcal{O}(2NM)$  flops. Alternatively, the addition of more Stokeslets in a method similar to the method of images [12, 13, 14] would require  $\mathcal{O}(2SN)$  operations to compute the added velocity, where  $S$  is the number of added Stokeslets. Our added velocity is computed in  $2N$  flops, making it much more efficient than any of these alternative methods.

The pressure throughout the domain can be computed using Eq. (2.5) without any modifications. If the domain is discretized on an  $m \times n$  grid, this calculation is

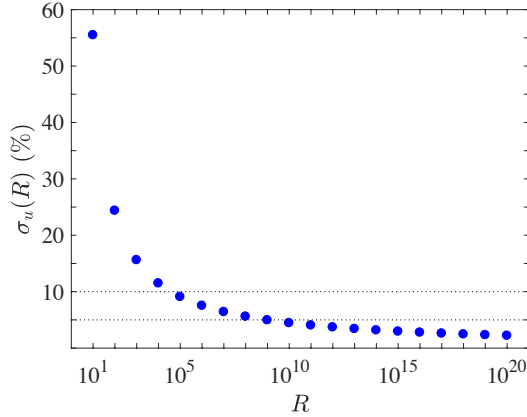


FIG. 2. Variation of the velocity on the large circle  $\Gamma$  for different values of  $R$ . Dotted lines indicate 10% and 5% variation.

$\mathcal{O}(mnN)$ . Alternative methods [25] exist that more efficiently compute the pressure throughout the domain of flow. However, since we only compute the pressure for visualization purposes (the values are not necessary to track the motion of the points  $\mathbf{x}_k$ ), and do so infrequently, we use the much simpler Eq. (2.5) to compute the pressure.

**3.1. Choosing the radius.** Central to our method is the assumption that the velocity computed from Eq. (2.9) on the large circle  $\Gamma$  is relatively constant. The validity of this assumption dictates a typical value of  $R$ . In order to test the variation of the velocity on the large circle  $\Gamma$ , we first impose a force of  $\mathbf{f}_0 = \begin{pmatrix} 1 \\ 0 \end{pmatrix}$  at the origin. Next, we use Eq. (2.9) to compute and measure the velocity from the Stokeslet (i.e. the velocity without the addition of  $\mathbf{u}^R$ ) on the large circle.

Specifically, we discretize the circle  $\Gamma$  with  $N = 100$  points and quantify velocity variability by defining

$$(3.2) \quad \sigma_u(R) = \left| \frac{\max_i u_x - \min_i u_x}{\bar{u}_x} \right|.$$

Here the index  $i$  runs from 1 to  $N = 100$ ,  $u_x$  refers to the velocity in the  $x$  direction (the direction of the force), and  $\bar{u}_x$  refers to the arithmetic mean of  $u_x$  taken over  $\Gamma$ .

Fig. 2 shows the values of  $\sigma_u(R)$  (as a percentage) for different values of  $R$ . We observe a variation in the velocity  $< 10\%$  for  $R \geq 10^5$  and a variation  $< 5\%$  for  $R \geq 10^9$ . In general, we use  $R = 10^{16} - 10^{17}$ , where the variation in the velocity is approximately 3%. In this case, our assumption that the velocity is approximately constant on the large circle is valid, and we can proceed with the scheme in Eq. (3.1).

**4. Examples.** We apply our method to three model systems of cells immersed in fluid, where the model equations have unbalanced forces. The cell consists of an elastic membrane immersed in fluid with the force unbalance generally occurring in a small region. We first consider a motile cell being driven by a rear contraction. Next, we examine a system in which the cell migrates through two flexible fibers. We conclude by studying pressure dynamics in cells with blebs, or small protrusions that are often used in migration. In all cases, all of the objects are flexible so that no boundary conditions are provided from the physics of each model system.

**4.1. Model of cell motility.** Cell crawling is an essential process for wound healing, cancer metastasis, and immune responses [26]. Cell migration is driven partially by actomyosin contractility, the process by which myosin molecular motors slide cytoskeletal actin filaments with respect to each other. This process typically occurs at the rear of migrating cells. For example, in fish keratocytes rear contraction combines with the protrusion of the cell's leading edge via actin polymerization to generate a clear leading and trailing side of the cell when viewed in two dimensions. Prior models of cell motility [26, 27] have used force balance equations to determine the motion of the cell. Here we impose a spatially localized contractile force at the rear of the cell to represent actomyosin contractility and couple these forces to those of an elastic membrane immersed in viscous flow. Our simplified model follows [4], where the force imbalance represents a protrusive actin network force that drives the cell's motion (represented by  $\mathbf{F}_{\text{net}}$  in [4]). Although substrate adhesion is not explicitly accounted for in our model, including a drag term similar to the one in [27] would simply result in smaller cell speeds without changing the key model outputs (e.g. steady state cell shape). The goal of our model is to determine the strength of contractile forces necessary to obtain realistic cell shapes and crawling speeds.

We model a keratocyte as an elastic membrane of radius  $R_m = 12.1$  (corresponding to the area reported in [27]) that is initially in a circular configuration. Letting  $s$  be the arclength coordinate that describes the membrane, the force density due to fiber elasticity is given by

$$(4.1) \quad \mathbf{F}^{el} = \frac{\partial}{\partial s} (T\boldsymbol{\tau}),$$

where  $\boldsymbol{\tau} = \mathbf{X}_s / \|\mathbf{X}_s\|$  is the unit vector tangent to the boundary and

$$(4.2) \quad T = \gamma_m + k_m(\|\mathbf{X}_s\| - 1)$$

is the fiber tension. The parameters  $\gamma_m$  and  $k_m$  represent membrane tension and stiffness. We use the values of 40 and 100 pN/ $\mu\text{m}$  for each, respectively [28].

We model contraction due to myosin via tangential contractile forces at the rear of the membrane. In particular, the total force on the membrane is the sum of fiber elasticity, Eq. (4.1), plus a contracting force at the back of the cell with force density

$$(4.3) \quad \mathbf{F}^{cont} = \begin{cases} F_{max} \begin{pmatrix} -\sin \theta \\ \cos \theta \end{pmatrix} & 0 < \theta - \pi < \pi/6 \\ F_{max} \begin{pmatrix} \sin \theta \\ -\cos \theta \end{pmatrix} & -\pi/6 < \theta - \pi < 0 \\ \mathbf{0} & \theta - \pi = 0, |\theta - \pi| \geq \pi/6 \end{cases}.$$

Here  $\theta = s/R_m$  is the angle measured counterclockwise from the  $x$  axis. The force applied to the cell is shown in Fig. 3(a). The unbalanced force comes from the underlying myosin activity due to ATP hydrolysis, which is a non-equilibrium process that constantly consumes energy [20]. The net contractile force due to myosin was estimated to be  $\mathcal{O}(10) - \mathcal{O}(100)$  pN in [27].

We discretize the membrane with  $N = 100$  points and simulate its motion through the fluid, which represents the internal cytoplasm containing actin polymers and the external fluid environment. Because of the large drag force on the keratocyte (due to adhesion to the substrate), we take the total system viscosity to be the shear

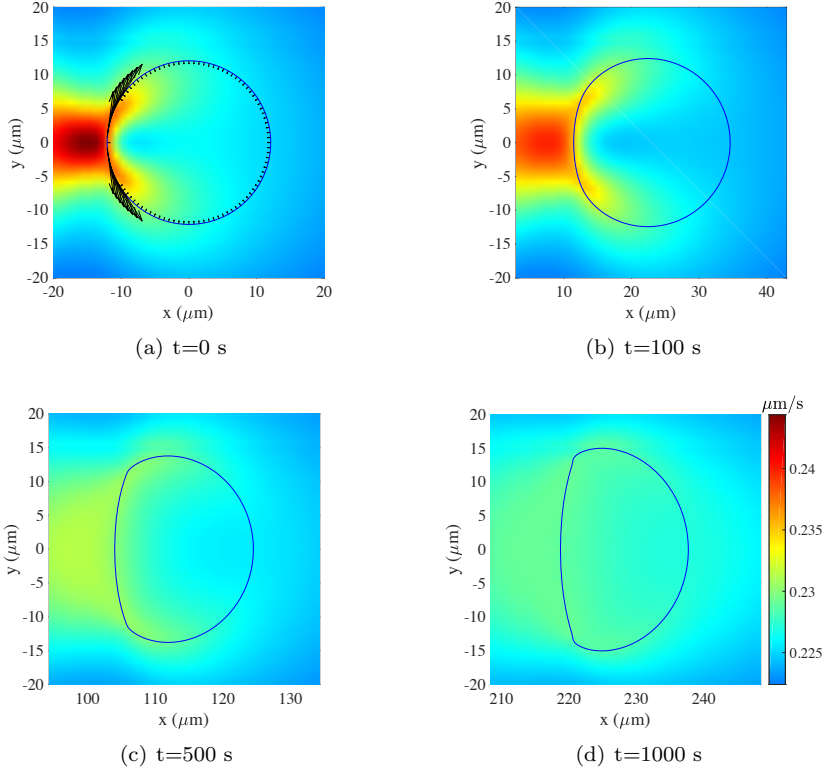


FIG. 3. Evolving shape and horizontal velocity dynamics for the motile cell with  $F_{max} = 50$   $\text{pN}/\mu\text{m}^2$ . The profiles are shown at  $t = 0, 100, 500,$  and  $1000$  seconds (the applied force is shown at  $t = 0$  as well). The horizontal velocity becomes more uniform as the cell approaches a steady state configuration.

viscosity of actin,  $\mu = 2000$  Pa·s from [27]. The velocity is computed from Eq. (3.1) with  $\epsilon = \Delta s$ . A forward Euler time update is used to advance the position of the cell with  $\Delta t = 1$  s.

We note that this model results in a net hydrodynamic force in the horizontal direction. From Eq. (2.8), the net hydrodynamic force in the positive direction gives an unbounded velocity in the negative horizontal direction at infinity. This spurious velocity at infinity affects the local velocity profile computed with Eq. (2.6), and the cell velocity computed without the added velocity in Eq. (2.18) is actually *backwards*. Only when we add the velocity in Eq. (2.18) does the cell move forward, as expected.

Fig. 3 shows the shape and horizontal velocity dynamics of a cell being pushed through the substrate with  $F_{max} = 50$   $\text{pN}/\mu\text{m}^2$ . As the cell moves through the fluid, the initial rapid velocity at the back of the cell equilibrates throughout the domain, and the cell achieves a steady state shape around  $t = 1000$  s (measured as the time when the difference between the maximum and minimum cell velocities is less than 15% of its initial value). We note that the steady state shape and velocity of approximately  $0.2$   $\mu\text{m}/\text{s}$  match those found experimentally in [27].

As discussed in [27], the force  $F_{max}$  and therefore the resulting steady state shape and velocity can change because of differences in the magnitude of adhesive and contractive forces on the cell. We therefore simulate the motion of the cell for  $F_{max} =$

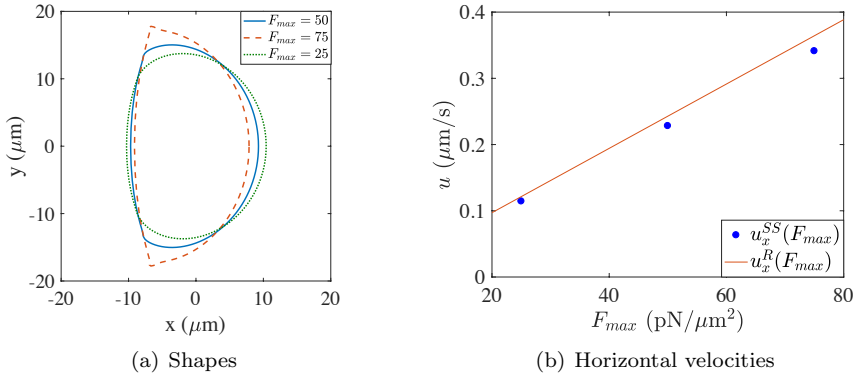


FIG. 4. Steady state shapes (a) and horizontal velocities (b) for the pushed cell. In (b), the total horizontal velocity is shown with blue circles, and the contribution from Eq. (2.18) is denoted by a red line.

25, 50 and 75  $\text{pN}/\mu\text{m}^2$  and compare the steady state shape and velocity dynamics. As shown in Fig. 4(a), the steady state shape appears more broad for lower values of  $F_{max}$ . When  $F_{max} = 75 \text{ pN}/\mu\text{m}^2$ , we observe unphysical corner-like edges developing in the cell for this large value of  $F_{max}$ .

Fig. 4(b) shows the steady state velocity in the horizontal direction as a function of  $F_{max}$ . We observe a linear relationship, as expected for the Stokes equations. We note how the contribution of  $\mathbf{u}^{\mathbf{R}}$  in Eq. (2.18) (shown in red) is slightly larger than the total velocity in Eq. (3.1), which indicates that the regularized Stokeslet velocity (second term in Eq. (3.1)) is actually backwards. This backward velocity, which grows with the force strength, shows why the corrective velocity  $\mathbf{u}^{\mathbf{R}}$  is necessary.

**4.2. Cell passing through fibers.** The cell being pulled through a system of fibers is a model for 3D cell migration and cancer cell metastasis. For example, cancer cells must migrate through a porous extracellular matrix or the walls of a blood vessel when metastasizing [29, 30, 31]. Previous studies have treated the extracellular tissue as rigid [31] or used an immersed boundary approach to model the cell moving through a system of fibers in the Navier-Stokes regime [32]. We seek to model a physically realistic set of stiff, but flexible, fibers in Stokes flow. We enforce the stiffness using a penalty-based tether force.

Denoting the prescribed configuration of a fiber as  $\mathbf{Z}(s)$ , the tether force density is given by

$$(4.4) \quad \mathbf{F}^{teth} = -k_{teth}(\mathbf{X}(s) - \mathbf{Z}(s)),$$

where the tether stiffness,  $k_{teth}$  ( $\text{pN}/\mu\text{m}^3$ ), is representative of the flexibility or bending rigidity of the fiber. In our simulations, we position two circular fibers of radius  $r_f = 5 \mu\text{m}$  with centers at  $(15, \pm 10.5)$ . The force on the fibers is given by a sum of Eqs. (4.1) and (4.4).

We simulate a membrane with radius  $9 \mu\text{m}$  (representative of a migrating cancer cell [31]) that is initially centered at  $(0, 0)$ . The force on the membrane comes from the sum of fiber elasticity, Eq. (4.1), and a pulling force on the front edge of the cell. The pulling force represents the growth of a polarized actin network at the leading

edge [26] and has density

$$(4.5) \quad \mathbf{F}^{pull} = \begin{cases} F_{max} \begin{pmatrix} \cos 6\theta \\ 0 \end{pmatrix} & |\theta| < \pi/12 \\ \mathbf{0} & |\theta| \geq \pi/12 \end{cases},$$

where  $F_{max} = 50 \text{ pN}/\mu\text{m}^2$ . We take the tension and stiffness of the membrane to be 40 and 100  $\text{pN}/\mu\text{m}$  respectively, as in Section 4.1. Since the fibers are much stiffer than the membrane, we take their stiffness to be 1000  $\text{pN}/\mu\text{m}$  (with no tension term). The interaction between the fibers and cell membrane takes place solely through the fluid, which has a viscosity of 0.27  $\text{Pa}\cdot\text{s}$  on both the inside and outside of the cell. This value has been previously used in the study of glioma cell migration [32].

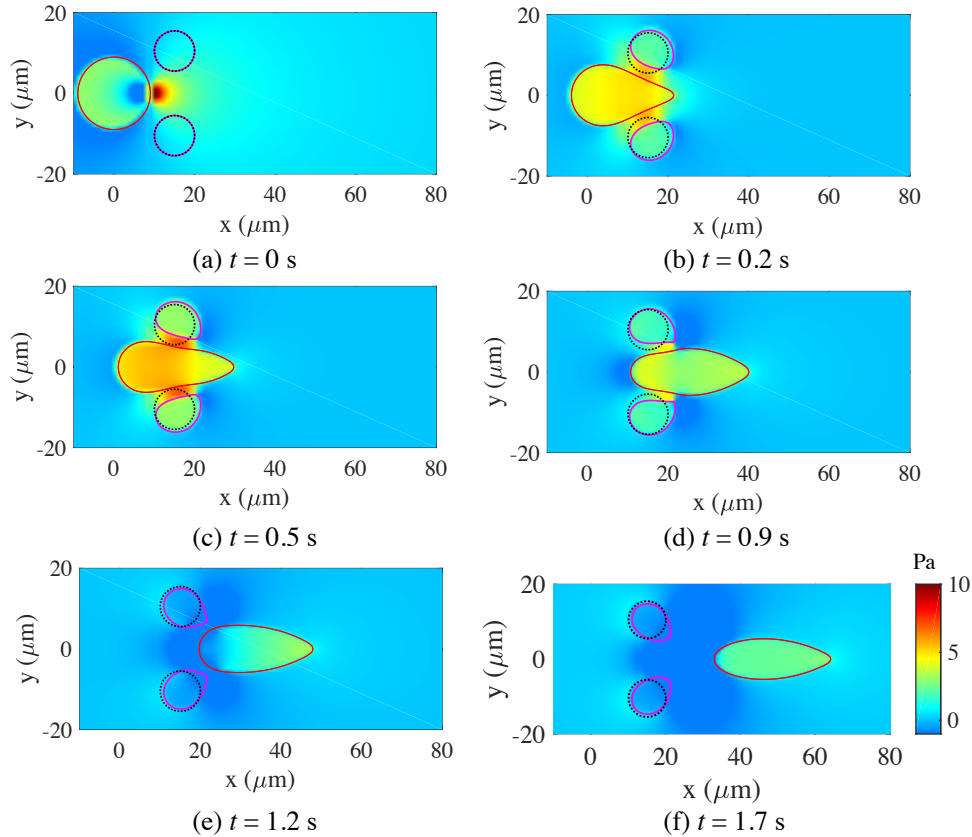


FIG. 5. Evolving shape and pressure dynamics for the cell pulled through 2 fibers with  $F_{max} = 50 \text{ pN}/\mu\text{m}^2$ . The profiles are shown at  $t=0, 0.2, 0.5, 0.9, 1.2,$  and  $1.7$  seconds. Dotted black lines show the fiber reference configuration while solid magenta lines show the deformed fibers. Note the pressure increase between the fibers as the cell passes through them.

Fig. 5 shows time values of the position of the cell membrane and corresponding pressure as the cell is pulled through the fibers with  $k_{teth} = 10 \text{ pN}/\mu\text{m}^3$ . As expected, we observe a combination of the membrane shape change and fiber motion allowing the membrane to pass through the fibers. As the membrane passes through the fibers, pressure builds up between them, resulting in a flow that aids in discharging the

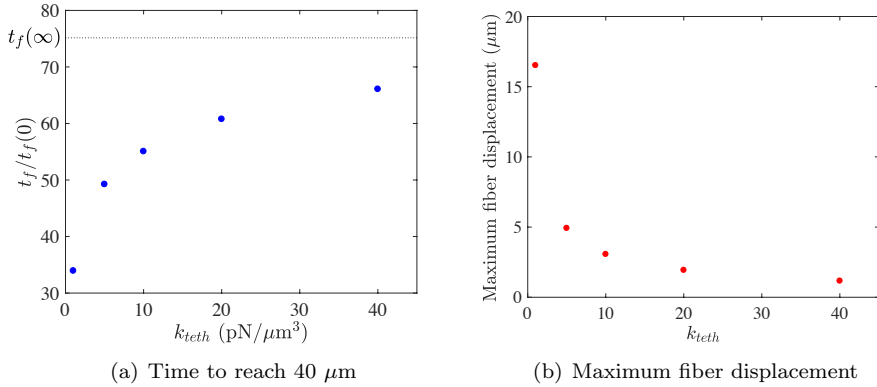


FIG. 6. Sensitivity analysis on  $k_{teth}$ . (a) shows the amount of time required for the cell to pass the line  $x = 40 \mu\text{m}$  as a function of  $k_{teth}$ , normalized by the 0.033 seconds required when no fibers are present. The line at  $t_f(\infty)$  is the corresponding ratio for rigid fibers. (b) shows the maximum fiber displacement for different values of  $k_{teth}$ . For both (a) and (b), the values chosen are  $k_{teth} = 1, 5, 10, 20, \text{ and } 40 \text{ pN}/\mu\text{m}^3$ .

membrane from the gap. Once the cell moves far away from the fibers, the pressure equilibrates to be uniform inside the cell and zero outside of it.

In order to determine the effect of the fiber stiffness on the cell migration time, we define  $t_f(k_{teth})$  as the time it takes for the entire cell to pass the vertical line  $x = 40 \mu\text{m}$  for a given value of the tether spring constant. In the absence of the fibers,  $t_f(0) = 0.033 \text{ s}$ . Fig. 6(a) shows the values of  $t_f$ , normalized by  $t_f(0)$  for  $k_{teth} = 1, 5, 10, 20, \text{ and } 40 \text{ pN}/\mu\text{m}^3$ . As expected, larger values of the fiber stiffness yield longer times for the cell to travel through the gap. In order to get an idea of how much the fibers actually deform for a given  $k_{teth}$ , Fig. 6(b) shows the maximum fiber displacement as a function of  $k_{teth}$ . For  $k_{teth} \geq 20 \text{ pN}/\mu\text{m}^3$ , the maximum displacement is less than or equal to  $2 \mu\text{m}$ . The displacement decays exponentially to this value.

For comparison, we simulate the membrane passing through two *rigid* fibers. In that case, a  $\mathbf{u} = 0$  boundary condition can be enforced on the fibers, and the method from [10] can be used without modifications. Denoting this case by  $k_{teth} = \infty$  (and the corresponding time as  $t_f(\infty)$ ), we observe in Fig. 6(a) that  $t_f(k_{teth} = 40)$  is 12% less than  $t_f(\infty)$ , despite the fact that the fibers only move a distance of  $\approx 1 \mu\text{m}$  in the former case. We conclude that the measured time for the cell to pass through the gap is quite sensitive to the amount of motion of the fibers. Modeling the flexible fibers as rigid will therefore introduce larger errors than expected when compared to experiments that use flexible environments, such as polyacrylamide gels [33]. Our formulation is advantageous in the case of flexible fibers because the  $k_{teth}$  parameter can be tuned based on the amount of fiber motion observed experimentally.

**4.3. Cellular blebbing.** Cellular blebs are spherical membrane protrusions that have been observed during cell migration [34]. A bleb forms when the cell cortex, a thin actin polymer elastic shell that is normally attached to the cell membrane by linker proteins, detaches from the membrane. Cells that bleb are pressurized due to actomyosin contractility in the cortex. Once a bleb is initiated, a pressure driven flow drives the intracellular fluid (cytoplasm) that locally expands the membrane.

Bleb initiation has been modeled using different approaches, including solid me-

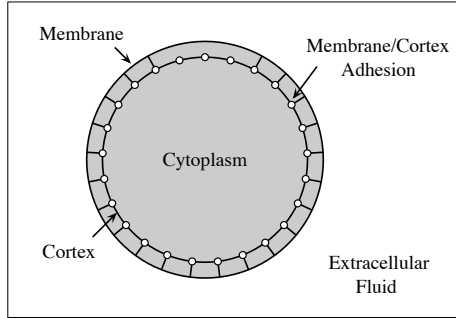


FIG. 7. Components of the bleb model. The cytoplasm is modeled as a viscous fluid. A bleb is initiated by removing membrane-cortex adhesive links in a small region at the top of the cell.

chanics [35], the immersed boundary (IB) method [28, 36], and boundary integral methods [5, 37, 38]. Results from several of these models have shown a bleb relieves only a small amount of intracellular pressure when the cytoplasm is modeled as a viscous fluid [36, 39]. Results from other models simulated with boundary integral methods show large pressure relief after bleb expansion [5, 37, 38]. Our goal is to identify the source of this contradiction because maintaining high intracellular pressure is essential for cells to migrate using blebs [40].

Here we present a model of bleb expansion based on [5]. We treat both the membrane and cortex as one dimensional curves with arclength parameter  $s$ . The force density (force/length) due to elasticity on both is computed by Eq. (4.1). The most critical part of the model is the adhesion that connects the membrane and cortex. We model adhesion by an elastic spring connecting the membrane to the cortex with stiffness  $k_{adh}$ . The force density on the membrane due to adhesion is given by,

$$(4.6) \quad \mathbf{F}_{adh}^{mem/cor}(s) = -k_{adh} (\mathbf{X}^m(s) - \mathbf{X}^c(s)),$$

with the force density on the cortex,  $\mathbf{F}_{adh}^{cor/mem}(s)$ , equal and opposite. Elastic forces on the membrane and cortex are due to surface tension and stretching. Tension is computed via Eq. (4.2) with constants  $\gamma_m$  and  $k_m$  representing membrane surface tension and stiffness, respectively. The corresponding elastic parameters for the cortex are denoted by  $\gamma_c$  and  $k_c$ . The membrane satisfies a no slip boundary condition, and its velocity is computed by Eq. (3.1). The velocity of the cortex is computed via a force balance, similar to [5],

$$(4.7) \quad \frac{d\mathbf{X}^c}{dt} = \frac{1}{\nu_c} (\mathbf{F}_{el}^{cor} + \mathbf{F}_{adh}^{cor/mem}),$$

where  $\nu_c$  is the cortical viscosity. A bleb is initiated by removing the adhesive links in a small region of length approximately  $5 \mu\text{m}$  at the top of the cell (see Fig. 7).

This particular blebbing model is a physical example where the net force on the membrane fiber is nonzero. When the links between the top of the membrane and cortex are broken, there is a net vertical force on the membrane because part of the adhesive forces acting in the negative vertical direction are no longer present. Even though the cortex feels the equal and opposite forces, it moves independently of the fluid according to Eq. (4.7). The net hydrodynamic force is therefore equal to the net force on the membrane, and is nonzero. Without including the constant velocity from Eq. (2.18), the membrane will escape from the domain because of a

Symbol	Quantity	Value	Source
$r_{\text{mem}}$	Cell radius	10 $\mu\text{m}$	[28, 39]
$r_{\text{cortex}}$	Cortex radius	9.9 or 9.85 $\mu\text{m}$	[38]
$\gamma_m$	Membrane surface tension	40 $\text{pN}/\mu\text{m}$	[28]
$k_m$	Membrane stiffness	80 $\text{pN}/\mu\text{m}$	
$\gamma_c$	Cortex surface tension	250 $\text{pN}/\mu\text{m}$	[36]
$k_c$	Cortical stiffness	100 $\text{pN}/\mu\text{m}$	[36]
$k_{\text{adh}}^{\text{mem/cortex}}$	Membrane/cortex adhesion stiffness coefficient	247 $\text{pN}/\mu\text{m}^3$	
$\mu$	Cytosolic viscosity	5 Pa-s	[36]
$\nu_c$	Cortical viscosity	10 $\text{pN-s}/\mu\text{m}^3$	[36]

TABLE 1  
Parameters for the blebbing model.

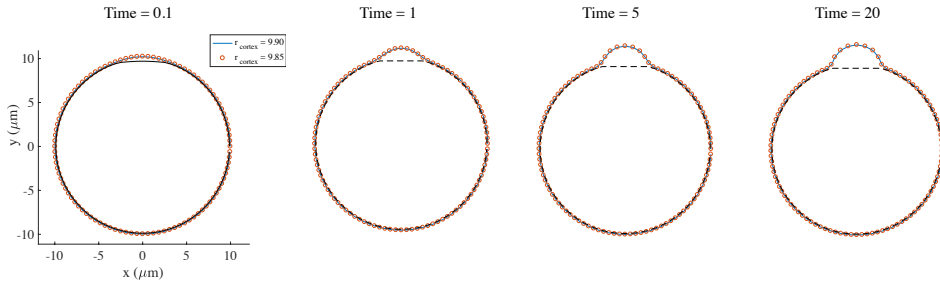


FIG. 8. Membrane position for a blebbing cell with initial cortex radius 9.90  $\mu\text{m}$  (blue line) or 9.85  $\mu\text{m}$  (red circles). The position of the cortex is shown as a dashed black line and is in approximately the same position in both simulations. The positions are shown at several time values after bleb initiation.

spurious downward velocity resulting from the force imbalance in the positive vertical direction and consequent failure to satisfy the velocity boundary condition at infinity. The addition of  $\mathbf{u}^R$  results in a well-posed problem so that we may solve for the membrane position in the blebbing model using the method of regularized Stokeslets.

Although previous studies have used the method of regularized Stokeslets to simulate cellular blebbing and migration in 2D [5, 37], the authors did not specify how they addressed the force imbalance in their models. We found our approach to give near identical results to a model where the net zero force constraint is enforced by subtracting at each Stokeslet point the mean of the calculated forces. However, the latter approach is non-unique since the opposite net force could also be imposed anywhere within the domain of flow by adding additional Stokeslets.

We simulate the cellular blebbing process with the parameters in Table 1. The two different values of the cortex radius are used to test our hypothesis that a force imbalance on the *cortex* is what drives the pressure relief seen by previous authors [5, 37, 38]. For  $k_{\text{adh}} = 247 \text{ pN}/\mu\text{m}^3$ , the forces on the cortex (in the absence of a bleb) are exactly in balance when  $r_{\text{cortex}} = 9.9 \mu\text{m}$ . When  $r_{\text{cortex}} = 9.85 \mu\text{m}$ , there is initially a force imbalance on the cortex independent of bleb initiation.

We first equilibrate the model for ten time steps, then initiate a bleb at  $t = 0$  by breaking the adhesion at the 7 (out of  $N = 100$ ) points with largest  $y$  coordinate.

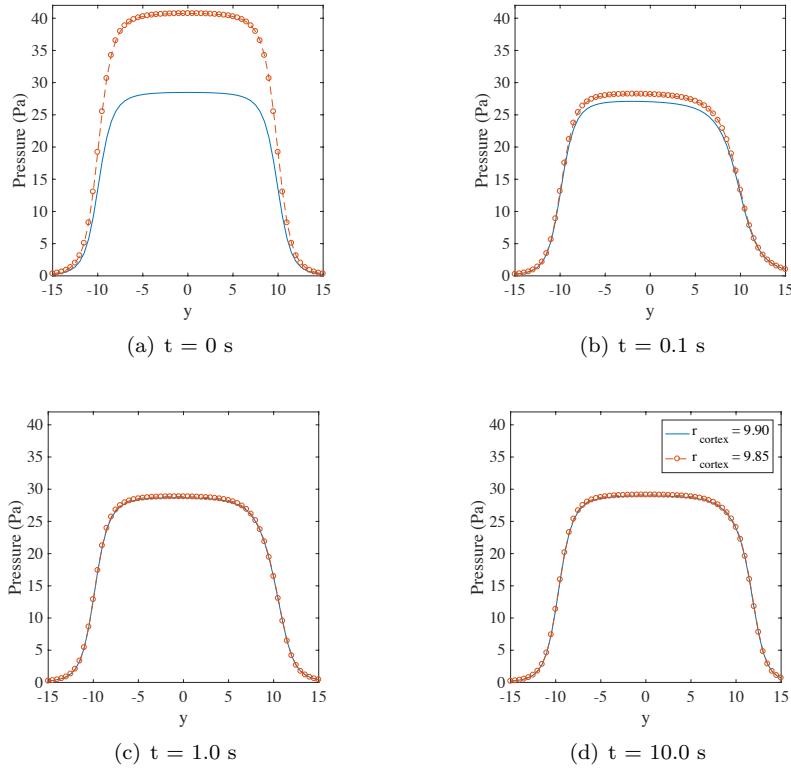


FIG. 9. Pressure profile along the line  $x = 0$  for the blebbing cell with initial cortex radius  $9.90 \mu\text{m}$  (blue line) or  $9.85 \mu\text{m}$  (red circles). Profiles are shown at (a)  $t=0 \text{ s}$ , (b)  $t=0.1 \text{ s}$ , (c)  $t=1.0 \text{ s}$ , and (d)  $t=10.0 \text{ s}$ . Note the large pressure relief when the forces are initially unbalanced on the cortex ( $r_{\text{cortex}} = 9.85$ ).

Fig. 8 shows the membrane shape over time for the two different values of the cortex radius, where time units are reported after bleb initiation. The bleb sizes and shapes are exactly the same. Despite this, the pressure dynamics of the two models are quite different. As shown in Fig. 9, the pressure drops significantly when  $r_{\text{cortex}} = 9.85$  but remains constant in the case  $r_{\text{cortex}} = 9.90$ . This is because of the force imbalance on the cortex in the former case. When the cortex's initial position is inwards of its resting position, it expands outward dynamically. This decreases the force on the membrane (and on the fluid) due to membrane-cortex adhesion (Eq. (4.6)), leading to a global pressure decrease inside the cell. Importantly, we observe that at  $t \geq 1 \text{ s}$ , the cortex has reached its resting position and the two pressures profiles are the same.

Models that include dynamic breaking of membrane-cortex adhesive links exhibit drastic changes in intracellular pressure [5, 38]. In such models, the dynamic breaking of adhesive links over time leads to pressure relief because the membrane force is updated suddenly without accounting for the corresponding force imbalance on the cortex. As the cortex slowly responds, it contracts inward in response to the loss of adhesive force, which promotes more link breakage and pressure changes. The cortex itself is therefore never truly in equilibrium, and the force imbalance on it drives

pressure changes.

The assumption that forces on the cortex are not equilibrated may be valid during highly dynamic processes such as during cell migration [41]. However, some experiments involve isolating a specific event, such as the expansion of a single bleb in [39]. In this work, experimental data show the cell achieves a quasi-steady state behavior after bleb expansion, and the cortex is unlikely to be dynamically relieving pressure.

**5. Conclusion.** When developing models for systems from biology, physics, and engineering that involve fluid-structure interaction, the simplification from 3D to 2D allows for model prototyping and fast simulations. In zero-Reynolds number flow, boundary integral methods are appealing because the velocity (and position) of immersed structures can be easily computed at the locations of interest rather than by interpolation after solving for the velocity on an Eulerian grid as in the IB method [23]. The condition of net zero force for 2D boundary integral methods can be a limiting factor during the development and simulation of mathematical models.

Here we present a numerical method to treat force constraints in 2D Stokes flow in an infinite domain. When the regularized or standard Stokeslet is used with a net nonzero hydrodynamic force in the flow domain, the velocity is unbounded at infinity (Stokes’ paradox). For problems where no specific boundary conditions are imposed from the physics of the model system, the standard Stokeslet solution without modification leads to unphysical velocities and is not mathematically valid. Available methods to treat this include requiring the net force to be zero within the domain and enforcing some boundary conditions to create a locally valid solution (previously treatments involve solving a linear system [4, 10, 42]). We show here that by combining the two conditions, a constant velocity can be obtained and added throughout the domain of flow. This additional velocity comes from the condition that the mean velocity over a large circle surrounding the domain be zero (i.e. a boundary condition). It also satisfies a type of force-free condition, specifically that the net force yielding the total velocity is zero. By imposing the “forces” (that yield the additional constant velocity) on a large circle far away from the domain, we can determine the relative velocity and pressure dynamics without having to apply the equal and opposite forces at arbitrary locations.

We apply our method to several models inspired by cell biology, where the model equations have net nonzero force. Models of cell motility with myosin contraction and actin polymerization have net force pulling or pushing the cell in a particular direction because of the interaction of myosin with the cytoskeleton in a non-equilibrium way [20]. In our model of a cell migrating through a tight junction, we show that our method allows for the use of tether forces that can be used to tune the flexibility of fibers or other immersed objects to experimental data. Finally, we use our model to infer how a force imbalance on the permeable cell cortex drives pressure relief (independent of bleb formation) in blebbing cells. Future work involves using our approach to investigate different mechanisms of cell migration through complex extracellular matrix architectures modeled by arrays of flexible fibers.

**6. Acknowledgements.** The authors thank Profs. Ricardo Cortez, Saverio Spagnolie, and Yoichiro Mori for helpful discussions. This work was supported by a grant from the Simons Foundation (#429808, Wanda Strychalski).

## REFERENCES

- [1] C. Pozrikidis, Numerical simulation of the flow-induced deformation of red blood cells, *Ann. Biomed. Eng.* 31 (10) (2003) 1194–1205. doi:10.1114/1.1617985.
- [2] C. Pozrikidis, Axisymmetric motion of a file of red blood cells through capillaries, *Phys. Fluids* 17 (3) (2005) 031503. doi:10.1063/1.1830484.
- [3] L. J. Fauci, R. Dillon, Biofluidmechanics of reproduction, *Annu. Rev. Fluid Mech.* 38 (2006) 371–394. doi:10.1146/annurev.fluid.37.061903.175725.
- [4] B. Vanderlei, J. J. Feng, L. Edelstein-Keshet, A computational model of cell polarization and motility coupling mechanics and biochemistry, *Multiscale Model. Sim.* 9 (4) (2011) 1420–1443. doi:10.1137/100815335.
- [5] F. Y. Lim, Y. L. Koon, K.-H. Chiam, A computational model of amoeboid cell migration, *Comput. Methods Biomech. Biomed. Engin.* 16 (10) (2013) 1085–1095. doi:10.1080/10255842.2012.757598.
- [6] L. H. Cisneros, R. Cortez, C. Dombrowski, R. E. Goldstein, J. O. Kessler, Fluid dynamics of self-propelled microorganisms, from individuals to concentrated populations, *Exp. Fluids* 43 (5) (2007) 737–753. doi:10.1007/s00348-007-0387-y.
- [7] E. Lauga, T. R. Powers, The hydrodynamics of swimming microorganisms, *Rep. Prog. Phys.* 72 (9) (2009) 096601. doi:10.1088/0034-4885/72/9/096601.
- [8] C. Pozrikidis, *Boundary integral and singularity methods for linearized viscous flow*, Cambridge University Press, 1992.
- [9] C. Pozrikidis, Interfacial dynamics for Stokes flow, *J. Comput. Phys.* 169 (2) (2001) 250–301. doi:10.1006/jcph.2000.6582.
- [10] R. Cortez, The method of regularized Stokeslets, *SIAM J. Sci. Comput.* 23 (4) (2001) 1204–1225. doi:10.1137/S106482750038146X.
- [11] G. Morra, Insights on the Physics of Stokes Flow, in: *Pythonic Geodynamics. Lecture Notes in Earth System Sciences*, Springer, 2018, pp. 93–104.
- [12] J. Blake, A note on the image system for a Stokeslet in a no-slip boundary, in: *Math. Proc. Cambridge*, Vol. 70, Cambridge University Press, 1971, pp. 303–310. doi:10.1017/S0305004100049902.
- [13] J. Ainley, S. Durkin, R. Embid, P. Boindala, R. Cortez, The method of images for regularized Stokeslets, *J. Comput. Phys.* 227 (9) (2008) 4600–4616. doi:10.1016/j.jcp.2008.01.032.
- [14] R. Cortez, D. Varela, A general system of images for regularized Stokeslets and other elements near a plane wall, *J. Comput. Phys.* 285 (2015) 41–54. doi:10.1016/j.jcp.2015.01.019.
- [15] A.-K. Tornberg, M. J. Shelley, Simulating the dynamics and interactions of flexible fibers in Stokes flows, *J. Comput. Phys.* 196 (1) (2004) 8–40. doi:10.1016/j.jcp.2003.10.017.
- [16] E. L. Bouzarth, A. T. Layton, Y.-N. Young, Modeling a semi-flexible filament in cellular Stokes flow using regularized Stokeslets, *Int. J. Numer. Meth. Bio.* 27 (12) (2011) 2021–2034. doi:10.1002/cnm.1454.
- [17] R. Cortez, M. Nicholas, Slender body theory for Stokes flows with regularized forces, *Comm. App. Math. Com. Sc.* 7 (1) (2012) 33–62. doi:10.2140/camcos.2012.7.33.
- [18] J. K. Wróbel, S. Lynch, A. Barrett, L. Fauci, R. Cortez, Enhanced flagellar swimming through a compliant viscoelastic network in Stokes flow, *J. Fluid Mech.* 792 (2016) 775–797. doi:10.1017/jfm.2016.99.
- [19] E. Nazockdast, A. Rahimian, D. Zorin, M. Shelley, A fast platform for simulating semi-flexible fiber suspensions applied to cell mechanics, *J. Comput. Phys.* 329 (2017) 173–209. doi:10.1016/j.jcp.2016.10.026.
- [20] J.-F. Joanny, J. Prost, Active gels as a description of the actin-myosin cytoskeleton, *HFSP J.* 3 (2) (2009) 94–104. doi:10.2976/1.3054712.
- [21] J. M. Teran, C. S. Peskin, Tether force constraints in Stokes flow by the immersed boundary method on a periodic domain, *SIAM J. Sci. Comput.* 31 (5) (2009) 3404–3416.
- [22] C. S. Peskin, Flow patterns around heart valves: a numerical method, *J. Comput. Phys.* 10 (2) (1972) 252–271. doi:10.1016/0021-9991(72)90065-4.
- [23] C. S. Peskin, The immersed boundary method, *Acta Numer.* 11 (2002) 479–517. doi:10.1017/S0962492902000077.
- [24] G. K. Batchelor, *An Introduction to Fluid Dynamics*, Cambridge University Press, 1967.
- [25] Y. Li, A. T. Layton, Accurate computation of Stokes flow driven by an open immersed interface, *J. Comput. Phys.* 231 (15) (2012) 5195–5215. doi:10.1016/j.jcp.2012.04.020.
- [26] B. Rubinstein, K. Jacobson, A. Mogilner, Multiscale two-dimensional modeling of a motile simple-shaped cell, *Multiscale Model. Sim.* 3 (2) (2005) 413–439. doi:10.1137/04060370X.
- [27] E. L. Barnhart, K.-C. Lee, K. Keren, A. Mogilner, J. A. Theriot, An adhesion-dependent switch between mechanisms that determine motile cell shape, *PLoS Biol.* 9 (5) (2011) e1001059.

- doi:0.1371/journal.pbio.1001059.
- [28] W. Strychalski, R. D. Guy, Intracellular pressure dynamics in blebbing cells, *Biophys. J.* 110 (5) (2016) 1168–1179. doi:10.1016/j.bpj.2016.01.012.
  - [29] D. G. Thomas, A. Yenepalli, C. M. Denais, A. Rape, J. R. Beach, Y.-I. Wang, W. P. Schiemann, H. Baskaran, J. Lammerding, T. T. Egelhoff, Non-muscle myosin IIB is critical for nuclear translocation during 3D invasion, *J. Cell Biol.* 10 (4) (2015) 583–594. doi:10.1083/jcb.201502039.
  - [30] C. M. Denais, R. M. Gilbert, P. Isermann, A. L. McGregor, M. te Lindert, B. Weigel, P. M. Davidson, P. Friedl, K. Wolf, J. Lammerding, Nuclear envelope rupture and repair during cancer cell migration, *Science* 352 (6283) (2016) 353–358. doi:10.1126/science.aad7297.
  - [31] L. Xiao, Y. Liu, S. Chen, B. Fu, Numerical simulation of a single cell passing through a narrow slit, *Biomech. Model. Mechan.* 15 (6) (2016) 1655–1667. doi:10.1007/s1023.
  - [32] W. Lee, S. Lim, Y. Kim, The role of myosin II in glioma invasion: A mathematical model, *PloS One* 12 (2) (2017) e0171312. doi:10.1371/journal.pone.0171312.
  - [33] R. W. Tilghman, C. R. Cowan, J. D. Mih, Y. Koryakina, D. Gioeli, J. K. Slack-Davis, B. R. Blackman, D. J. Tschumperlin, J. T. Parsons, Matrix rigidity regulates cancer cell growth and cellular phenotype, *PloS One* 5 (9) (2010) e12905. doi:10.1371/journal.pone.0012905.
  - [34] G. Charras, E. Paluch, Blebs lead the way: how to migrate without lamellipodia, *Nat. Rev. Mol. Cell Biol.* 9 (9) (2008) 730–736. doi:10.1038/nrm2453.
  - [35] T. E. Woolley, E. A. Gaffney, J. M. Oliver, R. E. Baker, S. L. Waters, A. Goriely, Cellular blebs: pressure-driven, axisymmetric, membrane protrusions, *Biomech. Model. Mechan.* 13 (2) (2014) 463–476. doi:10.1007/s10237-013-0509-9.
  - [36] W. Strychalski, R. D. Guy, A computational model of bleb formation, *Math. Med. Biol.* 30 (2) (2013) 115–130. doi:10.1093/imamb/dqr030.
  - [37] F. Y. Lim, K.-H. Chiam, L. Mahadevan, The size, shape, and dynamics of cellular blebs, *Europhys. Lett.* 100 (2) (2012) 28004. doi:10.1209/0295-5075/100/28004.
  - [38] C. Fang, T. Hui, X. Wei, X. Shao, Y. Lin, A combined experimental and theoretical investigation on cellular blebbing, *Sci. Rep.-U.K.* 7 (1) (2017) 16666. doi:10.1038/s41598-017-16825-0.
  - [39] J.-Y. Tinevez, U. Schulze, G. Salbreux, J. Roensch, J.-F. Joanny, E. Paluch, Role of cortical tension in bleb growth, *P. Natl. Acad. Sci. U.S.A.* 106 (44) (2009) 18581–18586. doi:10.1073/pnas.0903353106.
  - [40] E. K. Paluch, E. Raz, The role and regulation of blebs in cell migrations, *Curr. Opin. Cell Biol.* 25 (5) (2013) 582–590. doi:10.1016/j.ceb.2013.05.005.
  - [41] A. K. Yip, K.-H. Chiam, P. Matsudaira, Traction stress analysis and modeling reveal that amoeboid migration in confined spaces is accompanied by expansive forces and requires the structural integrity of the membrane–cortex interactions, *Integr. Biol.* 7 (10) (2015) 1196–1211. doi:10.1039/C4IB00245H.
  - [42] C. A. Copos, R. D. Guy, A porous viscoelastic model for the cell cytoskeleton, *ANZIAM J. forthcoming* (2018) 1–27 doi:10.1017/S1446181118000081.